A Programmable Platform for Accelerating the Development of Smart Ultrasound Transducer Probe

Xiaochen Xu, *Senior Member, IEEE*, Shabbir Amjhera Wala, Abhishek Vishwa, Jun Shen, Dijeesh K, Shriram Devi, Aatish Chandak, Sanjay Dixit, Elisa Granata, Sanjay Pithadia, Vajeed Nimran, and Sandeep Oswal, *Member, IEEE*

Abstract— During the COVID-19 pandemic, an ultraportable ultrasound smart probe has proven to be one of the few practical diagnostic and monitoring tools for doctors who are fully covered with personal protective equipment. The real-time, safety, ease of sanitization, and ultraportability features of an ultrasound smart probe make it extremely suitable for diagnosing COVID-19. In this article, we discuss the implementation of a smart probe designed according to the classic architecture of ultrasound scanners. The design balanced both performance and power consumption. This programmable platform for an ultrasound smart probe supports a 64-channel full digital beamformer. The platform's size is smaller than 10 cm × 5 cm. It achieves a 60-dBFS signal-to-noise ratio (SNR) and an average power consumption of ∼4 W with 80% power efficiency. The platform is capable of achieving triplex B-mode, M-mode, color, pulsed-wave Doppler mode imaging in real time. The hardware design files are available for researchers and engineers for further study, improvement or rapid commercialization of ultrasound smart probes to fight COVID-19.

Index Terms— Ultraportable ultrasound system, ultrasound for COVID-19, ultrasound smart probe.

I. INTRODUCTION

IN THE last decade, highly integrated system-on-chip devices have dropped in overall power consumption and size by 80%. This makes it possible to integrate most active electronics into an ultrasound probe. As a result, ultrasound smart transducers or probes, also called universal serial bus (USB) ultrasound probes or wireless ultrasound probes, can push ultrasound technology from niche radiology applications into daily point-of-care (POC) applications. During the COVID-19 pandemic, the ultraportable ultrasound smart probe has become one of only a few diagnostic and monitoring tools practical for use by doctors who are fully

covered with personal protective equipment (PPE), which makes it challenging to access other diagnostic tools [1]–[4].

Other imaging modalities, such as X-ray and computerized tomography (CT), are typical diagnostic tools when hospitals are not overwhelmed with COVID-19 patients. However, CT systems are usually available in top major hospitals in cities. And while X-ray systems are widely available in hospitals, radiation concerns make them unsuitable for continuous patient monitoring. Adding to these disadvantages, it takes about 15–30 min to obtain a set of CT images, and neither CT scan nor X-ray machines are common in intensive care units (ICUs) for monitoring COVID-19 patients. Under POC applications, quick in-field diagnosis and portability are the primary focuses. The 64- to 128-channel electronics in the POC ultrasound systems balance both portability and performance. Portable ultrasound systems with a transducer frequency of 3–13 MHz are convenient for both patients and doctors for diagnosing and monitoring lung disease at the bedside. Specific to the COVID-19 pandemic, ultrasound lung imaging helps doctors determine whether a patient should be admitted to the hospital and enables doctors to continue monitoring the lungs of admitted patients [3]–[7].

Compared to a laptop-size portable ultrasound system, ultrasound smart probes are even more suitable for COVID-19 diagnosis and monitoring. Cross-contamination between patients and doctors is avoided by the ability to sanitize the smart probes. Ultrasound smart probes are almost completely sealed; thus sanitization with 70% isopropyl alcohol is possible in a span of tens to less than 1 min. An ultrasound smart probe's ultraportability expands its usage scenarios from the ICU to the emergency room, from outpatient facilities to ambulances, and from top hospitals to countryside clinics.

In recent years, ultrasound smart probes have become much more affordable (<U.S. $2000), making them a viable option for most doctors and remote health care facilities. The current COVID-19 ultrasound lung imaging protocol recommends avoiding advanced imaging modes, such as harmonic imaging, frequency, and spatial compounding, and high mechanical index mode with high transmit energies. It is possible to obtain standardized images for artificial intelligence (AI) diagnosis. An inexpensive sealed ultrasound smart probe with long battery life and basic image features can be the ideal clinic

tool for fighting COVID-19 across the world, especially in developing countries [4], [7], [9]–[11].

Early researchers developed a smartphone-based single-channel Doppler system. Later, a smartphone-based low-channel-count ultrasound imaging system gained worldwide attention as an affordable diagnostic tool for developing countries [12]–[14]. Thus the demand to develop and optimize ultrasound smart probes has risen dramatically. Multiple research groups and companies have developed research systems to satisfy the needs of algorithm development, system optimization, and transducer characterization, but most systems are cart-based, and some ultraportable systems use components that are almost 10 years old [15]–[18]. Recently, researchers also discussed the feasibility of implementing advanced imaging methods into ultraportable systems [19], [20].

An opportunity exists for a leading-edge programmable platform for ultrasound smart probes to accelerate transducer optimization without cables, while minimizing electronic component count and supporting algorithm integration. For example, the approximately 2-m-long cable used in a typical ultrasound transducer contributes significant capacitance (100–150 pF), which represents the heavy load for high-voltage transmitters. In order to drive these heavy loads, transmitters are typically designed to deliver a 2-A peak current. Driving a heavy capacitive load also increases a transmitter's power consumption. Using inductors to maintain a resistive response at its resonance frequencies is necessary to tune out the additional cable capacitance. In a smart probe design, the elimination of long cable demands a more efficient transmitter with the correct amount of driving current, with an optimal chip size and power consumption. A programmable platform can evaluate how much driving current is necessary for different transducers by using the current programmability feature in transmitters. In addition, adjusting the on-board termination network at the inputs of receivers helps monitor and optimize the transducer's termination.

In this article, we describe the implementation of a smart probe designed according to the classic architecture of ultrasound scanners. This work included hardware design, performance evaluation, and imaging acquisition. We also analyzed the design specifications for lung imaging, such as overload recovery. The platform consists of 64 low-noise receiver channels, 128 transmitter channels, a field-programmable gate array (FPGA), and a USB controller. It includes power-management circuits to provide quiet supplies for received signals as low as tens peak-to-peak microvolts (μVpp) and for transmitting signals up to 160 Vpp. This platform is powered and accessed through a high-speed USB Type-C port available on most tablets or PCs. Radio frequency (RF) data are available for transducer characterization, power-consumption optimization, and algorithm development.

By setting corresponding transmitting patterns, the platform can also support synthetic aperture imaging, plane wave imaging, and conventional ultrasound imaging. In synthetic aperture imaging mode, it is possible to apply an N-cycle transmit pulse to each transducer element sequentially; in the plane wave imaging mode, you can apply N-cycle transmit pulses with appropriate delays to all 128 transducer elements simultaneously to form a steered beam; and in conventional imaging mode, applying delayed N-cycle transmit pulses to the corresponding 64-transducer elements to form a focused beam [19], [21].

We propose this system as a programmable hardware platform for researchers and developers to accelerate system design and optimization. A commercialized system based on this hardware platform would be possible for clinical diagnosis with additional design, test, and validation, and after obtaining approvals from corresponding government agencies.

II. Materials and Methods

A. System Architectures

Portable ultrasound systems typically have 64- to 128-channel transmitters and receivers and have been widely used in hospitals and by emergency response teams. Therefore, an ultrasound smart probe with a 64- to 128-channel beamformer is the ultimate goal to generate image quality comparable to portable systems. The power consumption, size, and thermal budget of a smart ultrasound probe limit the number of beamformer channels, however.

It is clear that a system tradeoff is necessary based on the availability, power consumption, and cost of the high-voltage transmitter and multiplexer, analog front end (AFE), and analog microbeamformer chips. Corresponding algorithm and imaging software development efforts can differ significantly depending on the selected architecture. Based on the simulation and discussion in [22]–[26], an ultrasound system with a 64-channel full-digital beamformer can achieve the optimal lateral resolution, contrast, and power consumption.

B. System Considerations for Lung Imaging

Both the air in the lungs and the ribs are perfect reflectors for ultrasound waves. But because strong reflected signals create challenges for producing clinical images with organ details, using ultrasound to image lungs is less common than X-ray or CT scans.

During the progression of COVID-19, doctors found that increasing amounts of fluid accumulate in the lungs as the pneumonia progresses. A lines (horizontal lines from multiple reflections) indicate normal lungs, while B lines (bright vertical streaks) indicate alterations of the lungs' surface. Experienced sonographers or trained AI machines can score the normality of the lungs based on the existence and combination of A lines and B lines. In addition, M-mode is common in lung imaging to visualize movements of the pleura line, A lines and lung tissue over time. M-mode lung images can have a unique seashore sign typically formed by these movements. Based on the visualization and analysis of the pleura line, A lines, B lines, and the seashore sign from both B-mode and M-mode images, it is possible to quickly assess lung for time-critical diagnosis and treatment [6].

Both A lines and B lines are caused by strong echo signals given the extreme mismatch of acoustic impedance between air and tissues or liquids. This means that the analog signal

chain must be able to recover from overload signals promptly and consistently. Although overload signals exist in blood-flow imaging due to a mismatch between the vessel walls and blood flow, a lung overload signal could be more than ten times higher due to the extremely low acoustic impedance of air. This means that the AFE must be able to passively attenuate the air-reflected signals before they enter the amplifier stage and amplify the attenuated overload signal promptly and consistently [27].

Keeping the design of the transmitter and its power-supply design very simple can help reduce overall system cost and size. Since COVID-19 lung imaging mainly uses B-mode and M-mode imaging, there are limited needs to dynamically reduce the transmitter voltage for Doppler modes. Typically, a highly integrated three-level transmitter with a fixed voltage is a good fit for lung imaging. A technique of using a three-level transmitter to dynamically ramp the supply voltage up and down will support Doppler modes. A transmitter with an integrated beamformer can free up hundreds of control pins from the FPGA and significantly simplify printed circuit board (PCB) routing.

C. System Implementation

The primary challenge in an ultrasound smart probe design is how to balance power consumption and performance. The most performance- and power-sensitive blocks are the transmitter, AFE, and FPGA. The AFE5832LP from Texas Instruments, Dallas, TX, USA, achieves 18.5 mW per channel at 4 nV/rtHz and 20 mega samples per second (MSPS), while the company's TX7332 achieves 16 mW per channel at ±70 V and a 0.1% duty cycle. Higher power consumption is expected when selecting a >20-MSPS sample rate or a > 0.1% duty cycle. The AFE5832LP samples up to 50 MSPS, and the TX7332 achieves >20 MHz at a −3-dB bandwidth, enabling support for high-frequency ultrasound (>20 MHz) applications. The Xilinx Artix-7 XC7A100T FPGA provides great performance per watt and has been proven in ultrasound applications, with a 15 mm × 15 mm footprint and 100 000 logic cells sufficient for a 64-channel ultrasound smart probe based on resource analysis [28]–[31].

We analyzed the performance of the clock distribution network in the FPGA and demonstrated that it could be used with 10- to 12-bit analog-to-digital converters (ADCs) used in most ultrasound applications. Other than the analog signal chain and digital processor, the USB Type-C (USB 3.1 Gen1) communication management chips (the Texas Instruments HD3SS3220 and Cypress FX3 CYUSB301X) provide high-speed data communication up to 5 Gb/s, which makes it possible to transfer ultrasound RF data quickly. Similar to cart-based ultrasound systems, ultrasound smart probes require the same amount of synchronized power supplies—from noise-sensitive signal chain power supplies to high-current digital supplies, from 1-V low-voltage supplies to ±80-V high-voltage supplies [32].

All devices in the design have flexible and fast power-up and power-down management to reduce the average power consumption through duty-cycle management. All of the devices satisfy the requirement of ∼4 W for an ultrasound smart
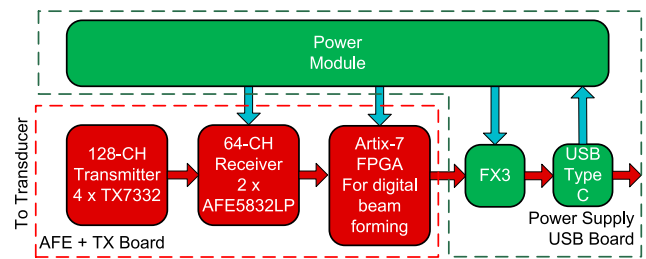

Fig. 1. Block diagram of the implemented ultrasound smart probe.

probe with a 64-channel digital beamformer. Figs. 1 and 2 are the block diagrams of the complete ultrasound smart probe and USB Type-C-based communication and power management, respectively. The dark red blocks in Fig. 2 indicate the power-management chips, including dc/dc power converters and low-dropout (LDO) regulators, which provide all supplies from 1 to +/−80 V for the AFE5832LP, TX7332, and XC7A100.

This power design generates a programmable bipolar supply up to ±80 V, from a very low input voltage (typically 5 V) in a single stage. Using a transformerless single-ended primary inductor converter (SEPIC) architecture meets key size and height constraints, while its high efficiency enables a low thermal footprint. This design also achieves <2% load regulation, fast transient response, and very low noise. The CDCE949 provides synchronized clocks for the dc/dc converters at the fixed frequencies of 500 and 250 kHz. The synchronized clock operation eliminates the frequency intermodulation if multiple clock sources exist in a system. The INA231s monitor the in-system current assumption and feedback to the imaging software to optimize performance and power consumption. The CYUSB301X handles data communication between the FPGA and a PC, mobile device, or notebook. The USB Type-C interface's rotationally symmetrical connector supports hot swap, but requires an HD3SS3220 port controller and TPD4E05U06 and TPD2EUSB30 electrostatic discharge protection chips, also made by Texas Instruments [32].

Fig. 3 shows the prototype system, which consists of two circuit boards. The top circuit board includes a 12-layer PCB with blind vias to stack four TX7332s on both the top and bottom layers. By stacking the TX7332s, the design incorporates more channels in a smaller volume, while placing two transmitter devices on opposite sides of the transceiver board and shorting pins with similar functions together uses less power. The transmit/receive switches in the channels of the two stacked transmitter devices can select which channels to transmit and receive signals from, such that signals from two channels with channel output pins shorted together are not compromised.

The transceiver board includes 128 transmitter channels and 64 receiver channels. When selecting the transmit/receive switch channel 65, the transmit/receive switch channel 1 remains open or at a high impedance during both signal transmission and reception; channel 65 operates normally to let received echoes pass to channel 1 of the AFE5832LP receivers, and vice versa. It is possible to short and couple the output pins for channel 65 and channel 1 to
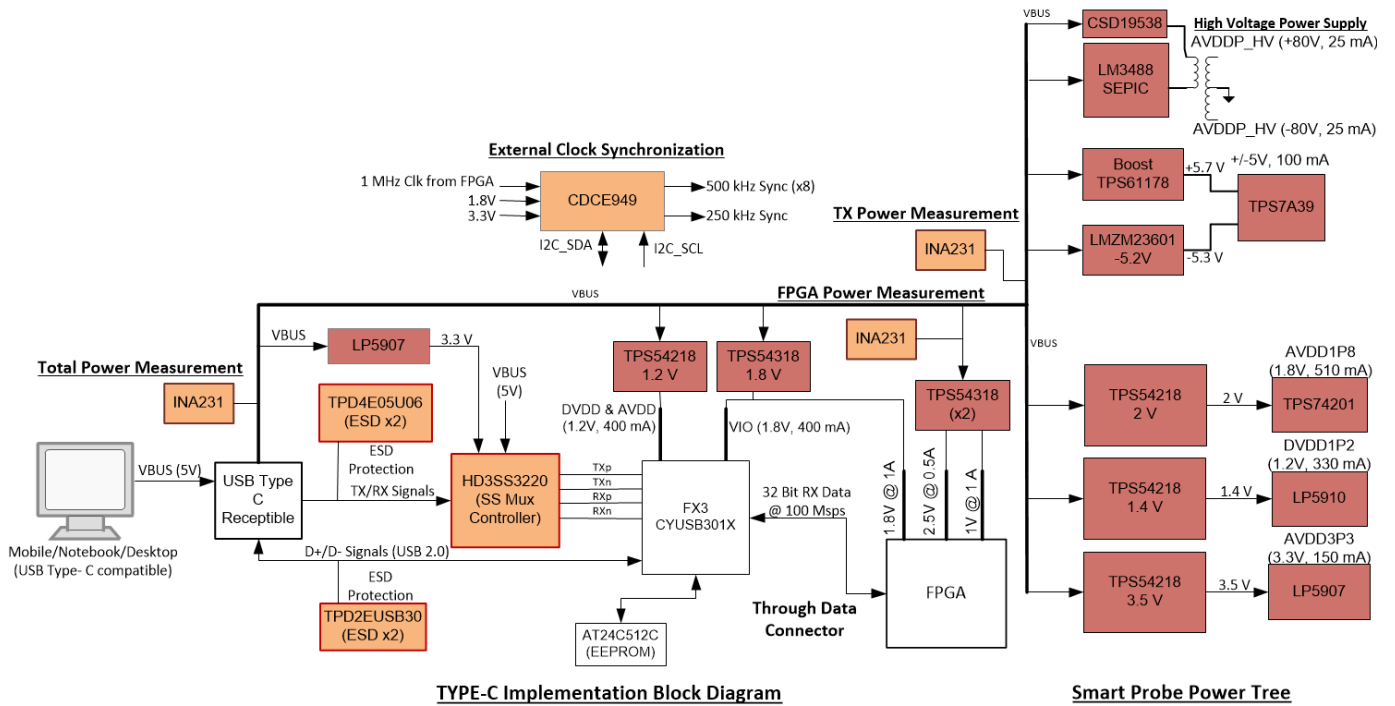
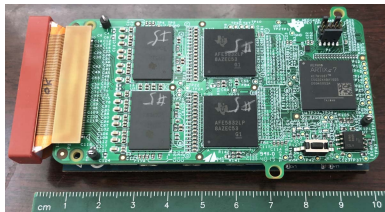Fig. 2. Block diagram of USB Type-C power management and communication.

Fig. 3. Programmable platform with a 128-element, 6-MHz linear array from Vermon S.A., Tours, France.

input channel 1 of the AFE5832LP receivers without comprising signal integrity. You can apply the same practice to channel N and $N+64$ accordingly. As a result, this configuration fully supports 128-element arrays whose active aperture is from element N to element $N+64$. When using a 64-element phased array, transmitter channels 65–128 can be completely powered down.

In addition, shorting the power-supply and receive pins of the two transmitter devices together reduces the number of blind vias needed and conserves the area on the transceiver board. A set of high-voltage supply capacitors are arranged on the top and bottom surfaces of the transceiver board near the transmitter devices, and a high-voltage supply local plane in the second layer of the transceiver board is aligned underneath the high-voltage supply capacitors to reduce supply plane parasitic inductance between the TX7332 transmitters and the high-voltage supply capacitors. The transceiver board also includes an FPGA to perform beamforming and beam steering operations on the received signals and form an ultrasound image. The bottom circuit board consists of a USB Type-C controller and all dc/dc power supplies. This board includes power-supply chips configured to provide a variety of different supply voltages to different devices on the transceiver board. The power-supply PCB is arranged underneath the transceiver board such that a high-voltage power submodule configured

to provide a large supply voltage for the TX7332 transmitters is close to the TX7332s.

A 3.5-MHz curved array and a 7.5-MHz lead zirconated titanate (PZT) linear array are the best fit for covering the frequency range used in lung imaging: 3–13 MHz. Vernon S.A., Tours, France, and ALS Inc., Shanghai, China, designed and manufactured the prototype transducer array heads. Single-crystal transducers have wider bandwidth. For example, the Philips eL18-4 transducer has an operation range of 2–22 MHz. A capacitive micromachined ultrasonic transducer (cMUT) can also achieve a very wide bandwidth [33], [34]. As a result, it is possible to use one probe to cover the full frequency range of 3–13 MHz in lung imaging and ensure easy operation in the field. In addition, the AFE5832LP's 50 MSPS sampling rate ensures a sufficient sampling resolution for wide-band transducers with a frequency as high as 25 MHz.

D. Software Control and Data Communication

The control software of this programmable platform is based on National Instruments' LabVIEW and the Python 2.7 programming language. Users have the flexibility to set custom transmit patterns, delays, aperture size and other specifications for traditional imaging, synthetic aperture imaging, or plane wave imaging. RF data acquired by the two AFE5832LPs are transferable to host a PC or a tablet offline for advanced algorithm development in MATLAB or other tools. Fig. 4 shows the software flowchart. Ecare Inc., Zhuhai, China, developed preliminary real-time imaging software and FPGA firmware.

III. RESULTS

A. Performance Evaluation

The main priority when designing an ultrasound smart probe is the power consumption, which is affected by the
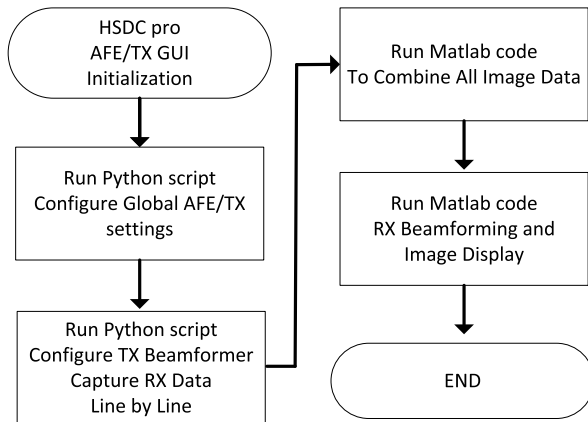
Fig. 4.   Flowchart for Python RF data collection and MATLAB post-processing.
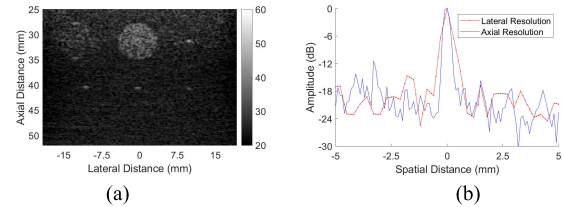

Fig. 5.   (a) Phantom B-mode image obtained offline after plane-wave transmission. (b) Wire target backscattered amplitudes showing the system's lateral and axial resolution.

TABLE I
POWER ANALYSIS OF THE OPEN PLATFORM

Block Name	Active Power	Idle Power	Conditions
2 x AFE5832LPs	1.64 W	64 mW	Fs=50MSPS, 10-bit
4 x TX7332s	0.66 W	26 mW	64-ch, 0.05% duty cycle
CLK Crystal	0.05 W	50 mW	Active all the time
FPGA General	0.83 W	150 mW	LVDS, clocking
FPGA Beamformer	0.6 W	0	Basic beamformer
USB	0.28 W	20 mW	
Total Power	4.1 W	410 mW	
Post Power Block	5 W	500 mW	80% Power Efficiency

constraints of probe size as well as temperature limitations. Table I shows the measured power numbers in active mode with 100% duty-cycle operation and in idle mode. The measured active circuit board surface temperature is about 60 °C. In clinical-use cases, the system duty cycle varies from 50% to 75%. It is feasible to adjust the overall operation duty cycle to achieve approximately 2.5–4 W of average power. Thus, it becomes possible to keep the surface temperature of the transducer below 45 °C. In some performance-driven applications, 5 W of power is also acceptable when implementing larger probe sizes or active cooling. In such cases, it is practical for designers to implement a premium smart probe with 128-channel transmitters and receivers, or to add a continuous-wave (CW) Doppler signal chain. The in-system power measurement was carried out by the Texas Instruments INA231 power monitor. A breakout power adaptor board measured each rail's power consumption during development.

The analog performance of the receiving signal chain will determine an ultrasound smart probe system's image quality. Texas Instruments high-speed data converter pro (HSDC Pro) software analyzed the analog performance of high-speed ADCs or AFEs [35]. Applying fast Fourier Transform (FFT) to the captured data calculates the signal-to-noise ratio (SNR) and total harmonic distortion (THD). The Keysight Technologies HP8642B synthesized signal generator generated a clean 5-MHz signal that was further filtered by a TTE Inc., Arcade, NY, USA, KC4T-5M 5-MHz passive bandpass filter with 5% bandwidth. We measured an SNR of 60 dBFS and a THD

of 55 dBFS with the HSDC Pro software. We also measured a crosstalk of −60 dBc without a connected transducer from the adjacent AFE channel, which did not have an input signal. Zhou *et al.* [36] reported a crosstalk in conventional PZT arrays is worse than −35 dBc. Thus, the transducer crosstalk limits the overall system crosstalk.

Using the metal–oxide–semiconductor field-effect transistor (MOSFET)-based transmit–receive switch (TRSW) in the TX7332, the passive attenuator before the amplifier and the high-pass filters in the AFE5832LP achieved fast and consistent overload recovery. Pulsed-wave Doppler or color Doppler modes acquired multiple image lines for extracting Doppler shift frequencies. Ideally, the data from these image lines are identical when there is no moving object; that is, the echo data remain the same and at the same depth of these image lines.

It is possible to define the deviation of image line data as the repeatability at a particular imaging depth, particularly analyzing the data of 128–64 image lines. The overload repeatability of the AFE5832LP under 2–3-Vpp input signals is equivalent to the AFE's thermal noise; that is, the deviation of data from image lines under overload is equivalent to the AFE's thermal noise. As a result, no additional Doppler noise is observed under overload. This excellent overload recovery ensures that the platform can handle strong signals reflected by air in the lungs, producing not only good imaging quality for lung imaging but also for general imaging in POC applications.

B. Preliminary Imaging Acquisition

The CIRS 040GSE ultrasonic phantom was used to evaluate the imaging capability of this system [37]. A 7.1-MHz one-cycle pulse was used to excite a 128-element 7.5-MHz linear array from ALS Inc. A phantom image with a single 0° plane-wave transmit setting shown in Fig. 5 demonstrated the entire flow from Python data capture to offline MATLAB processing. The measured −6-dB lateral and axial resolutions of the wire target at a depth of 31 mm are 550 and 390 μm, respectively. The following equation defines the contrast ratio [38] as:

$$\text{CR} = 20\log_{10}\left\{\frac{|\mu_{\text{in}} - \mu_{\text{out}}|}{\sqrt{(\sigma_{\text{in}}^2 + \sigma_{\text{out}}^2)/2}}\right\} \qquad (1)$$

where μ_{in} and μ_{out} represent the mean gray level inside and outside the gray scale target, and σ_{in} and σ_{out} are the standard deviations of the gray level inside and outside the gray scale target.

For contrast-ratio calculation, we selected two 25 × 25 pixel blocks inside and outside the middle grayscale target. The
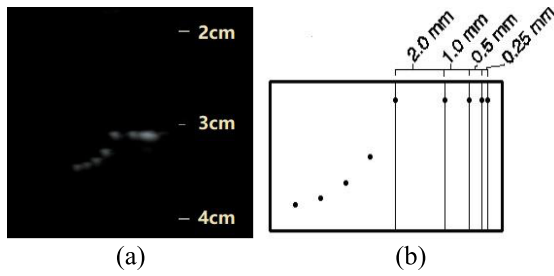
Fig. 6. (a) B-mode image of axial and lateral resolution targets, displaying a 42-dB dynamic range. (b) Axial and lateral pin targets with a distance step from 0.25 to 2 mm.
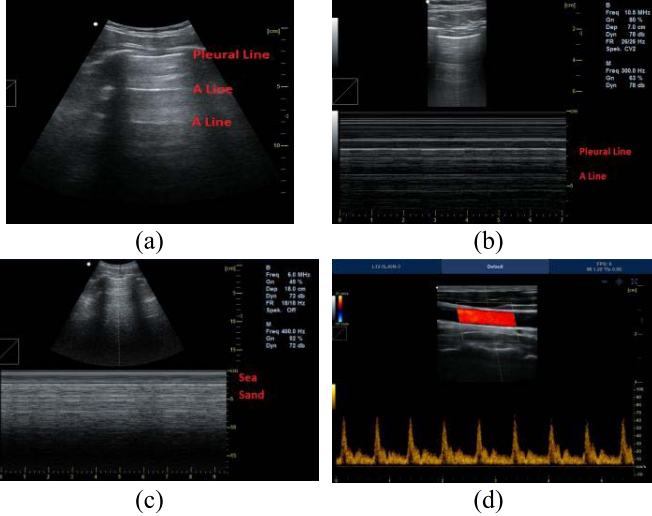

Fig. 7. (a) Normal lung image with A lines. (b) M-mode for monitoring the absence of lung sliding. (c) M-mode for indicating an aerated lung. (d) Triplex-mode neck image.

TABLE II
FPGA XC7A100T UTILIZATION REPORT

Resource	Utilization	Available	Utilization %
LUT	26469	63400	41.75
LUTRAM	5837	19000	30.72
FF	48822	126800	38.50
BRAM	133	135	98.52
DSP	177	240	73.75
IO	171	210	81.43
BUFG	8	32	25.00
MMCM	1	6	16.67

measured contrast ratio is 18 dB, which meets the >15-dB contrast ratio specification in the datasheet of the 040GSE ultrasonic phantom [37]. The imaging result is comparable to the same single $0°$ plane-wave image obtained from a Verasonics research platform [38], and is much better than the result from the ultraportable system in [17].

Ecare integrated the programmable platform architecture with the beamforming and imaging engine to obtain real-time images. The system achieved a frame rate of >30 frames/s, and each frame composites 128 B-mode image lines with a penetration of 15 cm. This frame rate is lower than the calculated ideal frame rate of 40 frames/s after considering the sound velocity of 1540 m/s, the imaging penetration of 15 cm and the 128 image lines per frame. Table II lists

TABLE III
COMPARISON OF ULTRAPORTABLE RESEARCH SYSTEMS

Name	Noise nV/rtHz	ADC CH No	Fs Msps	Power W	TX Vpp	PCB Size cm	Design Accessible
This work	3	64	50	5	160	10×5	Yes
Hager[16]	5.5	64	32.5	5.6	100	22×4.5	No
Ahn[17]	0.75	16	40	7.5	140	18×5.5	No
JH Kim[18]	?	32	40	5.5	120	14×5	No

the XC7A100T FPGA utilization report. The FPGA resources are sufficient for most smart ultrasound probe applications.

The block random access memory (BRAM) is the most used resource in order to support a phase array, which needs more beamforming configurations than a linear array. The frame-rate improvement from 30 frames/s to the ideal frame rate of 40 frames/s is limited by the total power consumption, the configuration time among image lines, and the FGPA resources.

Fig. 6(a) shows a B-mode image by using a Gammex ultrasonic 404GS phantom [39] and a 128-element 7.5-MHz linear array from ALS Inc. It indicates <1-mm lateral resolution and <0.5-mm axial resolution. Fig. 7(a) shows a normal lung image with A lines and a pleural line; Fig. 7(b) demonstrates a lung M-mode image; Fig. 7(c) indicates an aerated lung with a seashore line; and Fig. 7(d) shows a triplex mode neck image. These images demonstrate the platform's capability of real-time B-mode, M-mode, color mode, and pulsed-wave Doppler mode imaging.

IV. CONCLUSION AND DISCUSSION

Table III compares this programmable platform with the ultraportable systems in [16]–[18]. Table III lists the major analog specifications, the system board sizes without a transducer, and the design accessibility to researchers. Ahn *et al.* [17] illustrated a 16-channel smart probe with a power consumption of 7.5 W and a noise of 0.75 nV/rtHz; it achieved premium noise performance but created thermal challenges in the probe design. Kim *et al.* [18] doubled the channel count to 32 channels and reduced the power consumption to an acceptable range for a probe thermal design, although 32 channels are still much less than mainstream portable systems with a 64-channel digital beamformer. Hager's LightProbe [16] closed the gap on beamformer channel count, while clinical applications demand lower noise, a higher ADC sampling rate, and more transmitting power. In this article, this publicly accessible platform achieves 5.2-dB better sensitivity, 4 dB more transmitting power, and 50% smaller size than the latest LightProbe reported in [16], resulting in a total potential image contrast improvement of 9 dB.

Since most commercial ultraportable systems rarely publish their analog specifications, we briefly discussed comparing this platform and commercial ultraportable systems in terms of system specifications [16], [40]. This programmable platform supports 1–20-MHz piezoelectric ceramics transducers used by most commercial ultraportable systems. Similar to

commercial systems, this platform offers the same real time B-mode/M-mode/pulsed-wave Doppler mode/color Doppler mode imaging. The host machine can be either a PC or a tablet.

RF data accessibility and the programming flexibility of this platform are usually not available on commercial ultra-portable systems, but the former enables researchers to develop advanced applications such as automated ultrasound diagnostic information extraction and AI-assisted telemedicine [41]–[43]. We verified that this platform's high-speed USB Type-C interface exceeded 3.5 Gb/s, which can speed up the transferring of raw ADC RF data for research purposes. Compared to the design discussed in [16], however, this programmable platform without optical fiber transceivers does not support real-time RF data transferring, which requires a transfer rate greater than 15 Gb/s. Faster data transfer could be possible in the future by using the 20-Gb/s USB 3.2 Gen 2 $\times$ 2 or the 40-Gb/s USB 4.0 [44].

This article described a programmable platform for ultrasound smart probe to support a 64-channel fully digital beamformer. The programmable platform's hardware design files are available for researchers and engineers to study, improve, or streamline ultrasound smart probes development. This platform also can help support the development of next-generation ultrasound smart probes with software beamforming based on the Texas Instruments AFE58JD32LP, released in March 2020 [45], [46]. We expect that future AI diagnostic engines will provide not only efficient diagnoses but also real-time optimization feedback on the analog signal chain.

Contact the corresponding author to discuss using the programmable system in academic teaching or research. The design files shown in Fig. 2 are accessible at https://www.ti.com/tool/TIDA-010057. For the complete design source files, including schematic and layout files and source codes, e-mail mysecuresoftware_medical@list.ti.com.

ACKNOWLEDGMENT

REFERENCES

[1] G. Wang *et al.*, "Medical Imaging," in *Handbook of Research on Biomedical Engineering Education and Advanced Bioengineering Learning: Interdisciplinary Concepts*. Hershey, PA, USA: IGI Global, 2012, pp. 634–712.

[2] F. Ali *et al.*, "A narrative review on the advantages of portable ultrasound machines in the emergency department," *EC Emergency Med. Crit. Care*, vol. 2, no. 2, pp. 43–47, Sep. 2018.

[3] S. M. Newhouse, T. W. Effing, B. D. Dougherty, J. A. D' Costa, and A. R. Rose, "Is bigger really better comparison of ultraportable handheld ultrasound with standard point-of-care ultrasound for evaluating safe site identification and image quality prior to pleurocentesis," *Respiration*, vol. 99, no. 4, pp. 325–332, 2020, doi: 10.1159/000505698.

[4] X. Qian, R. Wodnicki, H. Kang, J. Zhang, H. Tchelepi, and Q. Zhou, "Current ultrasound technologies and instrumentation in the assessment and monitoring of COVID-19 positive patients," *IEEE Trans. Ultrason., Ferroelectr., Freq. Control*, vol. 67, no. 11, pp. 2230–2240, Nov. 2020, doi: 10.1109/TUFFC.2020.3020055.

[5] T. Zou, W. Yin, and Y. Kang, "Application of critical care ultrasound in patients with COVID-19: Our experience and perspective," *IEEE Trans. Ultrason., Ferroelectr., Freq. Control*, vol. 67, no. 11, pp. 2197–2206, Nov. 2020, doi: 10.1109/TUFFC.2020.3020628.

[6] L. R. Sultan and C. M. Sehgal, "A review of early experience in lung ultrasound in the diagnosis and management of COVID-19," *Ultrasound Med. Biol.*, vol. 46, no. 9, pp. 2530–2545, Sep. 2020, doi: 10.1016/j.ultrasmedbio.2020.05.012.

[7] A. C. H. Yu, L. Demi, M. Muller, and Q. Zhou, "Ultrasound imaging: A silent hero in COVID-19 and lung diagnostics," *IEEE Trans. Ultrason., Ferroelectr., Freq. Control*, vol. 67, no. 11, pp. 2194–2196, Nov. 2020, doi: 10.1109/TUFFC.2020.3031444.

[8] G. Soldati *et al.*, "Proposal for international standardization of the use of lung ultrasound for patients with COVID-19: A simple, quantitative, reproducible method," *J. Ultrasound Med.*, vol. 39, no. 7, pp. 1413–1419, Jul. 2020, doi: 10.1002/jum.15285.

[9] X. Liu, Y. Hai, B. Ma, B. Chong, and J. Liu, "Critical care ultrasonography and its application for COVID-19," *Adv. Ultrasound Diagnosis Therapy*, vol. 2, no. 2, pp. 43–49, Apr. 2020, doi: 10.37015/AUDT.2020.200035.

[10] E. Poggiali *et al.*, "Can lung US help critical care clinicians in the early diagnosis of novel coronavirus (COVID-19) pneumonia," *Radiology*, vol. 295, no. 3, p. E6, Jun. 2020, doi: 10.1148/radiol.2020200847.

[11] G. Cioni *et al.*, "A multisystem approach by bed-side ultrasound in patients with COVID-19 infection: A case series," *Italian J. Med.*, vol. 14, no. 2, pp. 106–111, Apr. 2020, doi: 10.4081/itjm.2020.1288.

[12] C.-C. Huang, P.-Y. Lee, P.-Y. Chen, and T.-Y. Liu, "Design and implementation of a smartphone-based portable ultrasound pulsed-wave Doppler device for blood flow measurement," *IEEE Trans. Ultrason., Ferroelectr., Freq. Control*, vol. 59, no. 1, pp. 182–188, Jan. 2012, doi: 10.1109/TUFFC.2012.2171.

[13] B. Jana, R. Biswas, P. K. Nath, G. Saha, and S. Banerjee, "Smartphone-based Point-of-Care system using continuous-wave portable Doppler," *IEEE Trans. Instrum. Meas.*, vol. 69, no. 10, pp. 8352–8361, Oct. 2020, doi: 10.1109/TIM.2020.2987654.

[14] *Ultrasound Imaging More Portable, Affordable With USB-Based Probes*. Accessed: Dec. 10, 2020. [Online]. Available: https://www.microsoft.com/en-us/research/wp-content/uploads/2016/02/en-us-collaboration-focus-health-msr_ultrasound.pdf

[15] E. Boni, A. C. H. Yu, S. Freear, J. A. Jensen, and P. Tortoli, "Ultrasound open platforms for next-generation imaging technique development," *IEEE Trans. Ultrason., Ferroelectr., Freq. Control*, vol. 65, no. 7, pp. 1078–1092, Jul. 2018, doi: 10.1109/TUFFC.2018.2844560.

[16] P. A. Hager and L. Benini, "LightProbe: A digital ultrasound probe for software-defined ultrafast imaging," *IEEE Trans. Ultrason., Ferroelectr., Freq. Control*, vol. 66, no. 4, pp. 747–760, Apr. 2019.

[17] S. Ahn *et al.*, "Smartphone-based portable ultrasound imaging system: Prototype implementation and evaluation," in *Proc. IEEE Int. Ultrason. Symp. (IUS)*, Oct. 2015, pp. 1–4, doi: 10.1109/ULTSYM.2015.0517.

[18] J. H. Kim, S. Yeo, M. Kim, S. Kye, Y. Lee, and T.-K. Song, "A smartphone based portable ultrasound imaging system for point-of-care applications," in *Proc. 10th Int. Congr. Image Signal Process., Biomed. Eng. Informat. (CISP-BMEI)*, Oct. 2017, pp. 1–5, doi: 10.1109/CISP-BMEI.2017.8302121.

[19] C. L. Palmer and O. M. H. Rindal, "Wireless, real-time plane-wave coherent compounding on an iPhone: A feasibility study," *IEEE Trans. Ultrason., Ferroelectr., Freq. Control*, vol. 66, no. 7, pp. 1222–1231, Jul. 2019, doi: 10.1109/TUFFC.2019.2914555.

[20] Z. Zhou, Y. Wang, Y. Guo, Y. Qi, and J. Yu, "Image quality improvement of hand-held ultrasound devices with a two-stage generative adversarial network," *IEEE Trans. Biomed. Eng.*, vol. 67, no. 1, pp. 298–311, Jan. 2020, doi: 10.1109/TBME.2019.2912986.

[21] J. A. Jensen, S. I. Nikolov, K. L. Gammelmark, and M. H. Pedersen, "Synthetic aperture ultrasound imaging," *Ultrasonics*, vol. 44, pp. e5–e15, Dec. 2006, doi: 10.1016/j.ultras.2006.07.017.

[22] *Ultrasound Imaging More Portable, Affordable With USB-Based Probes*. Accessed: Dec. 10, 2020. [Online]. Available: http://www.ti.com/lit/pdf/sboa361

[23] X. Xu *et al.*, "Open platform for accelerating smart ultrasound transducer probe development," in *Proc. IEEE Int. Ultrason. Symp. (IUS)*, Sep. 2020, pp. 1–4, doi: 10.1109/IUS46767.2020.9251594.

[24] J. A. Jensen, "Field: A program for simulating ultrasound systems," *Med. Biol. Eng. Comput.*, vol. 34, no. 1, pp. 351–353, Dec. 1995.

[25] J. A. Jensen and N. B. Svendsen, "Calculation of pressure fields from arbitrarily shaped, apodized, and excited ultrasound transducers," *IEEE Trans. Ultrason., Ferroelectr., Freq. Control*, vol. 39, no. 2, pp. 262–267, Mar. 1992, doi: 10.1109/58.139123.

[26] K.-Q. Zhao, T. G. Bjastad, and K. Kristoffersen, "Error analysis of subaperture processing in 1-D ultrasound arrays," *IEEE Trans. Ultrason., Ferroelectr., Freq. Control*, vol. 62, no. 4, pp. 663–672, Apr. 2015, doi: 10.1109/TUFFC.2014.006822.

[27] X. Xu, H. Venkataraman, S. Oswal, E. Bartolome, and K. Vasanth, "Challenges and considerations of analog front-ends design for portable ultrasound systems," in *Proc. IEEE Int. Ultrason. Symp.*, Oct. 2010, pp. 310–313, doi: 10.1109/ULTSYM.2010.5935843.

[28] *TX7332 Product Page*. Accessed: Dec. 10, 2020. [Online]. Available: http://www.ti.com/product/TX7332

[29] *AFE5832LP Product Page*. Accessed: Dec. 10, 2020. [Online]. Available: https://www.ti.com/product/AFE5832LP

[30] *Artix-7 Product Page*. Accessed: Dec. 10, 2020. [Online]. Available: https://www.xilinx.com/products/silicon-devices/fpga/artix-7.html

[31] *Low Cost Ultrasound*. Accessed: Dec. 10, 2020. [Online]. Available: https://www.xilinx.com/applications/medical/Low-Cost-Ultrasound.html

[32] *Designing Bipolar High Voltage SEPIC Supply for Ultrasound Smart Probe*. Accessed: Dec. 10, 2020. [Online]. Available: https://www.ti.com/lit/an/sloa284/sloa284.pdf

[33] *Ultrasound Probes & Transducers*. Accessed: Dec. 10, 2020. [Online]. Available: https://www.usa.philips.com/healthcare/solutions/ultrasound/ultrasound-transducer

[34] B. T. Khuri-Yakub and Ö. Oralkan, "Capacitive micromachined ultrasonic transducers for medical imaging and therapy," *J. Micromech. Microeng.*, vol. 21, no. 5, pp. 54004–54014, May 2011.

[35] *High-Speed Data Converter Pro Software*. Accessed: Dec. 10, 2020. [Online]. Available: https://www.ti.com/tool/DATACONVERTERPRO-SW

[36] S. Zhou, G. L. Wojcik, and J. A. Hossack, "An approach for reducing adjacent element crosstalk in ultrasound arrays," *IEEE Trans. Ultrason., Ferroelectr., Freq. Control*, vol. 50, no. 12, pp. 1752–1761, Dec. 2003, doi: 10.1109/TUFFC.2003.1256316.

[37] *Multi-Purpose, Multi-Tissue Ultrasound Phantom Model 040GSE*. Accessed: Dec. 10, 2020. http://www.cirsinc.com/wp-content/uploads/2020/03/040GSE-DS-032320-1.pdf

[38] H. Liebgott, A. Rodriguez-Molares, F. Cervenansky, J. A. Jensen, and O. Bernard, "Plane-wave imaging challenge in medical ultrasound," in *Proc. IEEE Int. Ultrason. Symp. (IUS)*, Sep. 2016, pp. 1–4, doi: 10.1109/ULTSYM.2016.7728908.

[39] *404GS LE Precision Small Parts Grey Scale Phantom*. Accessed: Dec. 10, 2020. [Online]. Available: https://biomedequip.com/image/data/PDF/006288-00-09_404_GS_LE.pdf

[40] B. A. Liu, M. D. Xu, F. Faium, and M. D. Liu, "CMUT/CMOS-based butterfly iQ-A portable personal sonoscope," *Adv. Ultrasound Diagnosis Therapy*, vol. 3, no. 3, pp. 115–118, 2019.

[41] C. Baloescu *et al.*, "Automated lung ultrasound B-Line assessment using a deep learning algorithm," *IEEE Trans. Ultrason., Ferroelectr., Freq. Control*, vol. 67, no. 11, pp. 2312–2320, Nov. 2020, doi: 10.1109/TUFFC.2020.3002249.

[42] S. Wu *et al.*, "Pilot study of robot-assisted teleultrasound based on 5G network: A new feasible strategy for early imaging assessment during COVID-19 pandemic," *IEEE Trans. Ultrason., Ferroelectr., Freq. Control*, vol. 67, no. 11, pp. 2241–2248, Nov. 2020, doi: 10.1109/TUFFC.2020.3020721.

[43] L. Carrer *et al.*, "Automatic pleural line extraction and COVID-19 scoring from lung ultrasound data," *IEEE Trans. Ultrason., Ferroelectr., Freq. Control*, vol. 67, no. 11, pp. 2207–2217, Nov. 2020, doi: 10.1109/TUFFC.2020.3005512.

[44] *Universal Serial Bus 4 (USB4) Specification Version 1.0*, USB Promoter Group, Portland, OR, USA, Aug. 2019.

[45] J. Ma, K. Karadayi, M. Ali, and Y. Kim, "Software-based ultrasound phase rotation beamforming on multi-core DSP," in *Proc. IEEE Int. Ultrason. Symp.*, Oct. 2011, pp. 503–506, doi: 10.1109/ULTSYM.2011.0121.

[46] *AFE58JD32LP Product Page*. Accessed: Dec. 10, 2020. [Online]. Available: https://www.ti.com/product/AFE58JD32LP
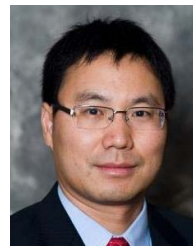
Xiaochen Xu (Senior Member, IEEE) received the B.S. degree in electrical engineering and the M.S. degree in acoustics from Nanjing University, Nanjing, China, in 1999 and 2002, respectively, and the Ph.D. degree in biomedical engineering from the University of Southern California, Los Angeles, CA, USA, in 2007.

He joined the Medical Business Unit, Texas Instruments, Dallas, TX, USA. He led the definition and development of analog ultrasound ICs, including low-noise analog front end and high-voltage transmitter chips. His research interests include ultrasound system design, integrated circuit definition and development, system-on-chip design and integration, and transducer design and applications.

Shabbir Amjhera Wala received the Bachelor of Technology and Master of Technology degrees both in microelectronics from IIT Bombay, Mumbai, India, in 2006 and 2008, respectively.

In 2008, he joined the Medical Business Unit, Texas Instruments, Bengaluru, India. He is leading all aspects of IC characterization, qualification, applications, reference design, probe test, final test, and customer engagement for ultrasound applications.

Abhishek Vishwa was born in Lucknow, India, in 1992. He received the Bachelor of Technology degree in electrical engineering and the Master of Technology degree in microelectronics from IIT Bombay, Mumbai, India, in 2017 and 2019, respectively.

He joined Texas Instruments, Bengaluru, India, in 2017, as a System Engineer within Medical Sector focusing on medical imaging and multiparameter patient monitoring systems. His area of interest includes analog design, mixed-signal design, industrial interfaces, and power supply design.

Jun Shen was born in Jiangxi, China, in 1989. He received the B.E. degree in microelectronics from the University of Electronic Science and Technology of China, Chengdu, China, in 2011, and the M.S. degree in microelectronics from the Huazhong University of Science and Technology, Wuhan, China, in 2014.

He is currently a Field Application Engineer with Texas Instruments, Shenzhen, China. His research interests include high integrated ultrasound transmitter and receiver.

Dijeesh K received the Bachelor of Technology degree from GEC Calicut, Kozhikode, India, in 2014 and the M.Tech. degree from the National Institute of Electronics and Information Technology Calicut, Kattangal, India, in 2019.

He joined Texas Instruments, Bengaluru, India, in 2018, as an Intern, where he is currently working as a Validation Engineer with the Motor Drive Team. He is focusing on brushed and stepper motor drivers. His responsibilities include designing the boards, validating the device, and customer debugs.

Shriram Devi received the Bachelor of Technology degree from the College of Engineering, Pune, India, in 2008 and the Master of Technology degree in electronic design from the Indian Institute of Science, Bengaluru, India, in 2012.

He joined the Medical Business Unit, Texas Instruments, Bengaluru, in 2008. He is involved in multiple aspects of product development cycle such as silicon validation, test, reference design, applications, and customer engagement. His interests include low-noise hardware design, field-programmable gate array (FPGA) development, and automation.

Aatish Chandak received the Bachelor of Technology degree in electronics and communication from NITK Surathkal, Mangalore, India, in 2015.

In 2015, he joined the Medical Business Unit, Texas Instruments, Bengaluru, India, as an Applications Engineer. He worked on characterization and applications support of the ultrasound devices. His research interests include analog and mixed circuit design, system, and reference design.

Sanjay Dixit has been working in multiple electronics companies in India, since 1994. Since 2016, he has been working as a Systems Engineer with the Medical System Team, Texas Instruments, Bengaluru, India. His main experience is in electronic system development.

Elisa Granata received the bachelor's and master's degrees in electronic engineering from the Polytechnic University of Milan, Milan, Italy, in 2016 and 2018, respectively.

She joined Texas Instruments (TI), Milan, in 2019, where she is currently a Field Application Engineer and also responsible for the technical support of industrial accounts, including medical customers.

Sanjay Pithadia has been with Texas Instruments (TI), Bengaluru, India, since 2008, where he is currently a System Engineer and is responsible for developing subsystem design solutions for medical applications. He has been involved in designing reference designs related to energy, smart grid, industrial motor drives, and medical imaging. He brings to this role his experience in analog design, mixed-signal design, industrial interfaces, and power supplies.

Vajeed Nimran received the Bachelor of Technology degree in electronics and communication engineering from the National Institute of Technology Calicut, Kozhikode, India, in 2004, and the master's degree in microelectronics from IIT Bombay, Mumbai, India, in 2007.

He was a Digital Designer with Freescale Semiconductor, Bengaluru, India. He joined the High Performance Analog Group, Texas Instruments (TI), Bengaluru. During his 13 years in TI, he has worked on various analog design blocks and products. He was the Main Designer for the ultrasound receive front-end analog front ends (AFEs), in-probe electronics for ultrasound probes, and different types of ultrasound transmitters.

Sandeep Oswal (Member, IEEE) received the Bachelor of Technology degree in electrical engineering from IIT Bombay, Mumbai, India, in 1994, and the master's degree in electrical engineering from The University of Texas at Austin (UT Austin), Austin, TX, USA, in 1997.

He joined Texas Instruments (TI), Bengaluru, India, in 1998. He started his career in TI in the broadband technology products working on the design and architecture of analog front end (AFE) for digital subscriber line (DSL) modems and high-speed data converters. Since 2007, he has been working in the area of medical AFE solutions. He has architected analog signal chains for portable and ultraportable ultrasound systems enabling differentiated system performance and size. He is currently a Technologist and a Signal Chain Architect with the Medical and Imaging Team, TI. In this role, he leads the architecture/process/design tradeoffs for front ends of medical imaging systems such as ultrasound, digital Xray, computerized tomography (CT), and front-end solutions for biosensing and patient monitoring applications. He specializes in signal chain front ends, A/D converters, and low-noise amplifiers. He holds 40 granted patents and 20 filed patents in the area of low-power analog circuit design and systems.